Available online at www.CivileJournal.org

Civil Engineering Journal

(E-ISSN: 2476-3055; ISSN: 2676-6957)

Vol. 11, No. 04, April, 2025

Crack Pattern Analysis and Reinforcement Strain Development in UHPSFRC-Strengthened RC Joints

Trung-Hieu Tran [1*]

[1] *Faculty of Civil Engineering, Hanoi Architectural University, Hanoi, Viet Nam.*

Received 02 January 2025; Revised 11 March 2025; Accepted 17 March 2025; Published 01 April 2025

Abstract

This study assesses the effectiveness of ultra-high performance steel fiber-reinforced concrete (UHPSFRC) in improving the seismic behavior of reinforced concrete (RC) exterior joints, emphasizing crack patterns and reinforcement strain development. Three full-scale specimens (a conventional RC control joint and two UHPSFRC-strengthened versions with 800 mm and 1025 mm strengthening lengths) were subjected to reversed cyclic loading to mimic seismic forces. Crack progression and strain distribution were examined through visual observations, strain gauges, and displacement data, offering a detailed evaluation of joint performance. Findings indicate that UHPSFRC enhances shear resistance, reduces crack widths significantly (<0.5 mm compared to >2 mm in the control), and modifies failure modes: the 800 mm length shifts damage to beam flexural failure, while the 1025 mm length increases peak capacity (231.4 kN vs. 185.8 kN) but reverts to joint shear failure. The novelty lies in UHPSFRC's ability to replace transverse reinforcement in congested joint zones, enhancing ductility and easing construction difficulties. This research provides fresh insights into optimizing UHPSFRC application length, delivering practical guidance for seismic retrofitting, and contributing to design standards for robust RC frames in seismic regions.

Keywords: Ultra-High Performance Concrete (UHPC); UHPSFRC; Exterior Joint; Reversed Cyclic Loading; Crack Pattern; Reinforcement Strain Development.

1. Introduction

The seismic performance of reinforced concrete (RC) frame structures is intricately tied to the behavior of beam-column joints, which serve as pivotal nodes for transferring forces between structural elements. The failure of these joints under cyclic loading can precipitate a cascade of damage, undermining the overall stability of the frame, even if beams and columns remain structurally sound [1]. Historical earthquakes, such as the 1995 Hyogo-Ken Nanbu event in Japan, the 1999 Kocaeli earthquake in Turkey, and the 2009 L'Aquila earthquake in Italy, have repeatedly demonstrated the vulnerability of RC joints, with post-event analyses attributing failures to insufficient shear capacity, inadequate transverse reinforcement, and poor anchorage of longitudinal bars. These incidents have highlighted the critical role of joints in ensuring the global integrity of RC frames, particularly in exterior connections where complex stress states—combining shear, bending, and axial forces—impose stringent demands on design and construction practices. Moreover, the growing frequency of seismic events globally has intensified the urgency to retrofit existing structures, many of which were built prior to modern seismic codes, to enhance their resilience against such forces [2-6]. A deeper analysis reveals that these joints often act as the weak link, with their brittle failure modes—driven by shear cracking and bond deterioration—exacerbating progressive collapse risks under repeated loading, a phenomenon insufficiently addressed by traditional design approaches. Recent studies, emphasize the efficacy of UHPSFRC jacketing in retrofitting bridge piers, suggesting its potential to similarly bolster joint resilience in RC frames [7-9].

* Corresponding author: hieutt@hau.edu.vn

http://dx.doi.org/10.28991/CEJ-2025-011-04-014

One of the persistent challenges in RC joint construction is achieving adequate concrete consolidation in regions congested with reinforcement. High longitudinal reinforcement ratios, often mandated by seismic codes to ensure strength and ductility, coupled with large bar diameters in beams, frequently obstruct concrete flow during casting. This issue is particularly acute in exterior joints involving slender columns, where the confined space exacerbates difficulties in maintaining anchorage and bond integrity. Such construction challenges not only compromise joint performance but also increase the likelihood of premature failure under seismic loading, as evidenced by field observations of poor concrete quality in joint cores [4]. Traditional solutions, such as increasing stirrup density or improving formwork techniques, often fall short in addressing these practical limitations, underscoring the need for innovative materials and approaches that enhance both structural capacity and constructability. Recent advancements in material science have thus shifted focus toward high-performance composites, offering promising alternatives to conventional methods by improving both strength and ease of application in retrofitting scenarios. However, a critical examination suggests that these traditional fixes often merely delay failure rather than fundamentally alter joint behavior, leaving a gap that advanced materials like UHPSFRC could fill by redefining load transfer mechanisms. For instance, Sai Kubair et al. [9] highlight UHPSFRC's enhanced fiber-matrix interfacial bonding as a key factor in improving seismic performance, addressing anchorage issues in congested zones.

Over the past few decades, advancements in concrete technology have introduced a range of high-performance materials aimed at overcoming these deficiencies. High-performance concrete (HPC), characterized by enhanced workability and strength, high-strength concrete (HSC), with compressive strengths exceeding 60 MPa, and fiber-reinforced concrete (FRC), incorporating fibers to improve tensile behavior, have been explored as alternatives to conventional concrete and steel stirrups in joint regions [6–11]. While these materials offer notable benefits—HPC improves placement, HSC boosts strength, and FRC enhances crack control—their application in seismic joints has revealed limitations. For instance, HSC often lacks the ductility required for energy dissipation under cyclic loading, and FRC may not fully replace transverse reinforcement in high-shear zones [12-14]. Moreover, the practical implementation of these materials is hindered by a scarcity of experimental data validating their performance under realistic loading conditions and a lack of standardized design guidelines, necessitating further research to bridge the gap between theoretical potential and field application. A broader analysis indicates that these materials, while incrementally beneficial, struggle to address the multifaceted demands of seismic joints—combining strength, ductility, and constructability—often resulting in trade-offs that limit their effectiveness in preventing catastrophic failure under extreme conditions. Recent work by Huang et al. [15] on hybrid fiber-reinforced concrete columns underscores the need for balanced material properties, a challenge UHPSFRC seeks to overcome.

Among these emerging materials, ultra-high performance concrete (UHPC) has emerged as a transformative option since its introduction in the early 21st century. UHPC boasts compressive strengths ranging from 150 to 200 MPa and tensile strengths of 8 to 15.9 MPa when reinforced with steel fibers, forming UHPSFRC [14–18]. This composite integrates UHPC's ultra-dense matrix—achieved through a low water-cement ratio (0.2–0.25), fine aggregates (<2.5 mm), and optimized particle packing—with steel fibers that enhance ductility, crack-bridging capacity, and bond strength with reinforcement [19–23]. These properties have led to its successful deployment in demanding applications worldwide, including pavements at Haneda Airport in Tokyo, the Gärtnerplatz Bridge in Kassel, Germany, and toll gates for the Millau Viaduct in France [24]. UHPSFRC's ability to reduce porosity, improve durability, and maintain performance in harsh environments positions it as a compelling solution for seismic joint strengthening. However, its adoption in RC structures remains limited by high material costs, complex production processes, and the absence of universally accepted design standards, which have slowed its integration into mainstream construction practices [25, 26]. Beyond its mechanical superiority, UHPSFRC offers a paradigm shift by enabling joints to absorb and dissipate energy more effectively, potentially transforming failure modes from brittle shear collapse to ductile yielding, a critical advantage over predecessors like HSC or FRC that warrants deeper exploration in seismic contexts. Valcuende et al. [27] demonstrate UHPSFRC's corrosion resistance under seismic loading, enhancing its long-term viability, while Shao et al. [28] reveal its superior bond behavior with steel reinforcement under cyclic loads, further supporting its seismic potential.

This study seeks to address these gaps by conducting a detailed experimental investigation into the performance of RC exterior joints strengthened with UHPSFRC under reversed cyclic loading. The research focuses on two key aspects: the evolution of crack patterns and the development of reinforcement strain, both of which are critical indicators of joint behavior under seismic conditions. By testing three full-scale specimens—a control joint and two UHPSFRC-strengthened variants with different strengthening lengths—this study evaluates how UHPSFRC influences shear resistance, crack control, and strain distribution. The findings aim to elucidate the material's potential in enhancing joint performance, overcoming construction challenges, and informing the development of design guidelines for seismic-resistant RC frames. Through this work, we contribute to the growing body of knowledge on advanced concrete composites, offering practical insights for engineers and researchers striving to improve structural resilience in earthquake-prone regions.

2. Methodology Overview

To ensure a systematic approach, this study followed a comprehensive methodology comprising the following key steps: (1) Design of test specimens based on standard RC frame configurations and seismic requirements, (2) Numerical modelling using ABAQUS in order to predict the responses of the RC frame; (3) Fabrication of specimens incorporating UHPSFRC at varying lengths (0 mm, 800 mm, and 1025 mm), (4) Instrumentation setup using strain gauges and LVDTs to collect crack and strain data, (5) Execution of reversed cyclic loading tests to simulate seismic forces, (6) Analysis of experimental results focusing on crack patterns and reinforcement strain, and (7) Development of a numerical model to validate and extend experimental findings. This workflow is illustrated in Figure 1 as a flowchart, providing a concise overview of the integrated experimental and numerical approach adopted in this research. In this figure, a feedback loop from step 6 to step 5 indicates iterative refinement based on experimental outcomes.

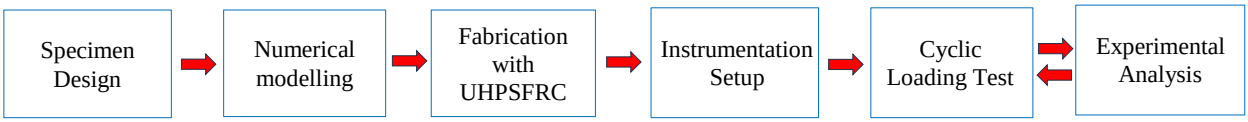

Figure 1. Flowchart of Research Methodology

3. Experimental Program

3.1. Test Specimen Details

The experimental program involved the design, fabrication, and testing of three full-scale RC exterior joint specimens, designated S1, S2, and S3, to assess the effectiveness of UHPSFRC in enhancing joint performance under reversed cyclic loading. The experimental program was designed to evaluate the seismic performance of reinforced concrete (RC) exterior beam-column joints under reversed cyclic loading, with a focus on the effectiveness of ultra-high performance steel fiber reinforced concrete (UHPSFRC) as a strengthening material. Three full-scale specimens, designated S1, S2, and S3, were constructed and tested to capture a range of behaviors under simulated seismic conditions. Specimen S1 was constructed as a control, representing a conventional RC joint with standard reinforcement detailing compliant with Vietnamese seismic standards, while S2 and S3 were modified versions strengthened with UHPSFRC in the joint region, with the transverse reinforcement (stirrups) entirely removed from the strengthened zones to assess the material's ability to replace conventional confinement methods, a key practical consideration for retrofitting congested joint areas. The specimens were designed to replicate typical exterior beam-column connections in RC frames, with identical overall geometric dimensions: beams measuring 350 mm wide by 450 mm deep and columns at 350 mm by 350 mm square.

All specimens shared identical overall geometric configurations to isolate the effect of UHPSFRC strengthening length. The beams measured 350 mm in width, 450 mm in depth, and 2000 mm in total length from the column face to the loading point, reflecting typical dimensions for mid-rise RC frame structures. The columns were square, with a cross-section of 350 mm × 350 mm and a height of 3000 mm (1500 mm above and below the joint centerline), ensuring sufficient length to simulate realistic boundary conditions. The joint itself was defined as the intersection zone, extending 350 mm vertically (column width) and 450 mm horizontally (beam depth) from the column face, consistent with standard exterior joint proportions. The primary variable across the specimens was the length of the UHPSFRC strengthening applied along the beam and joint: S1 had no UHPSFRC, S2 featured an 800 mm strengthened length, and S3 extended this to 1025 mm.

The reinforcement layout was consistent across all specimens to isolate the effect of UHPSFRC. Beams were reinforced longitudinally with two 25 mm and two 20 mm diameter bars at both top and bottom (total steel area of 1605 mm^2 per layer), while columns contained ten 20 mm diameter longitudinal bars (total steel area of 3140 mm^2). In S1, the beam's critical zone (within 500 mm of the column face) included stirrups in the beam's critical zone (near the joint) were 10 mm diameter bars spaced at 100 mm for S1 and S2, but absent in S3's strengthened region. Outside the critical zone, stirrups were spaced at 150 mm in all specimens. In the column, stirrups were placed at 80 mm spacing in the critical zone and 200 mm elsewhere. The joint region of S1 included six layers of 10 mm stirrups at 80 mm spacing, which were omitted in S2 and S3 due to UHPSFRC replacement. In S2, beam stirrups remained at 100 mm spacing outside the 800 mm UHPSFRC zone, while S3 had no stirrups within the 1025 mm strengthened length. An axial load of 650 kN was applied to the column top throughout testing, representing approximately 30% of the column's axial capacity (based on 30 MPa conventional concrete), to mimic typical service conditions in multi-story frames. Detailed configurations are summarized in Table 1, with geometric layouts depicted in Figure 2.

Table 1. Specimen Configurations

Component	Parameter	S1	S2	S3
Beam	Cross-section (mm)	350 × 450	350 × 450	350 × 450
	Longitudinal reinforcement	2d25 + 2d20	2d25 + 2d20	2d25 + 2d20
	Stirrups (critical zone)	d10@100	d10@100	-
	Stirrups (non-critical zone)	d10@150	d10@150	d10@150
	UHPSFRC length (mm)	-	800	1025
Column	Cross-section (mm)	350 × 350	350 × 350	350 × 350
	Longitudinal reinforcement	10d20	10d20	10d20
	Stirrups (critical zone)	d10@80	d10@80	d10@80
	Stirrups (non-critical zone)	d10@200	d10@200	d10@200
	UHPSFRC length (mm)	650	650	650
Joint	Stirrups	6 layers d10@80	-	-

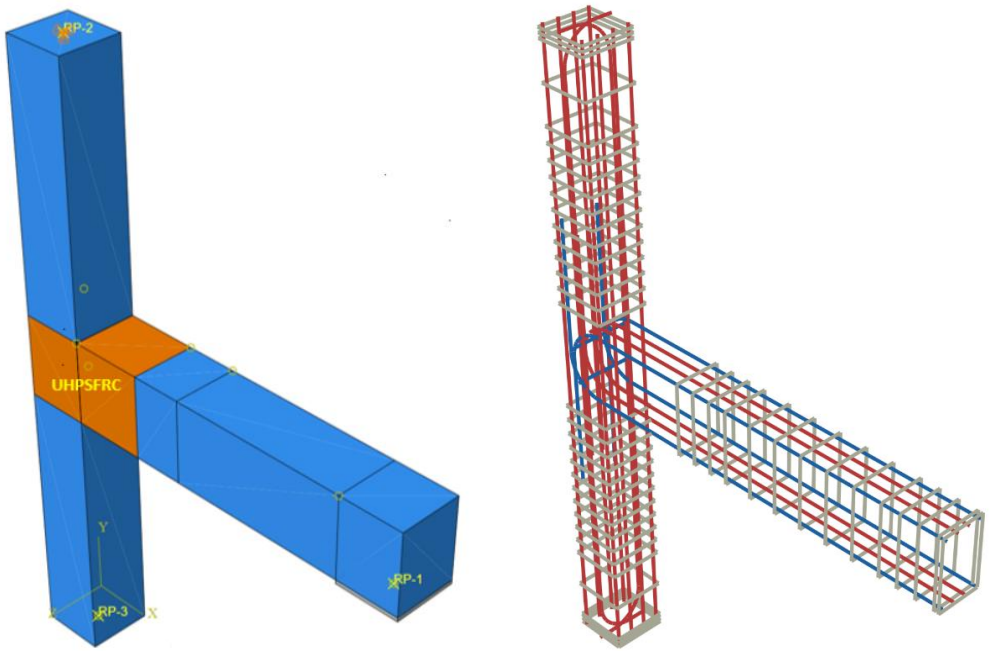

(a) Concrete layout (b) Reinforcement details

Figure 2. Geometric Dimensions of Test Specimens

3.2. Loading Protocol

The specimens were subjected to reversed cyclic loading to simulate seismic forces, applied using a hydraulic actuator with a 1000 kN capacity mounted at the beam end, 2000 mm from the column face. The loading setup was anchored to a stiff reaction frame, with the column base fixed to the laboratory strong floor via a steel hinge allowing rotation but restraining translation, and the column top restrained by a roller support permitting vertical movement while maintaining the 650 kN axial load via a secondary actuator. This configuration ensured that lateral cyclic loads were transferred through the beam to the joint, replicating the moment and shear demands experienced during earthquakes. The loading protocol followed a hybrid force-displacement approach adapted from ACI 374.1-05 guidelines, designed to progressively increase damage and assess seismic performance across a range of drift levels.

The loading sequence began with a force-controlled phase, applying increments of 20 kN up to the onset of cracking (approximately 50–80 kN, depending on the specimen), with three cycles at each load level to stabilize initial micro-cracking. Once visible cracks appeared—typically at the beam-column interface in S1 (50–60 kN) and at the UHPSFRC-concrete interface in S2 and S3 (70–80 kN)—the protocol shifted to displacement control. Displacement increments were based on drift ratios, starting at 0.25% (5 mm at the beam tip) and increasing in steps of 0.25%–0.5% (e.g., 0.75%, 1.0%, 1.4%, etc.) up to 6.5% (130 mm), with two cycles per drift level to capture hysteretic behavior and energy dissipation. The maximum drift of 6.5% was selected to exceed typical seismic design limits (e.g., 2–3% per FEMA 273), ensuring failure mechanisms were fully observed. Loading was applied at a quasi-static rate of 0.02 mm/s to minimize dynamic effects, with cycles reversed symmetrically to simulate bidirectional seismic action. During testing, environmental conditions were controlled within the laboratory, maintaining a temperature of 25 ± 3°C and relative

humidity of 60 ± 10%, monitored continuously with a calibrated environmental logger to ensure stability throughout the loading cycles. These conditions were selected to reflect typical indoor testing environments and prevent moisture loss or thermal effects from influencing crack propagation or strain measurements. The test concluded when specimens exhibited significant capacity loss (e.g., concrete crushing or rebar rupture), as observed at 5.0% drift for S1 and 6.5% for S2 and S3. This detailed setup and protocol provided a robust framework for evaluating crack progression, strain development, and failure modes, offering insights into UHPSFRC's seismic enhancement capabilities.

3.3. Material Properties

The reinforcement used in this study consisted of CB400-V grade steel bars manufactured by Hoa Phat (Vietnam), compliant with high ductility class (DCH) requirements per Vietnamese standards. Three bar diameters were employed: 10 mm for stirrups, and 20 mm and 25 mm for longitudinal reinforcement in beams and columns. To characterize their mechanical properties, three samples of each diameter were tested in tension following TCVN 197-1:2014 [29] for ambient temperature testing and TCVN 1651-2:2008 [30] for ribbed reinforcement specifications. Tests were conducted using an SHT4306-W universal testing machine with a maximum capacity of 3000 kN, equipped with an extensometer providing ±0.1% accuracy. The average yield strength (f_y), ultimate strength (f_u), and elastic modulus (E_s) were determined and are presented in Table 2, with stress-strain curves provided in Figure 3.

Table 2. Mechanical Properties of Reinforcement

Diameter (mm)	Area (mm^2)	Yield Strength, f_y (MPa)	Ultimate Strength, f_u (MPa)	Elastic Modulus, E_s (GPa)	Note
10	50	585	701		Stirrups
20	314	577	695	200	Beam/Column long reinforcement
25	491	528	662		Beam long reinforcement

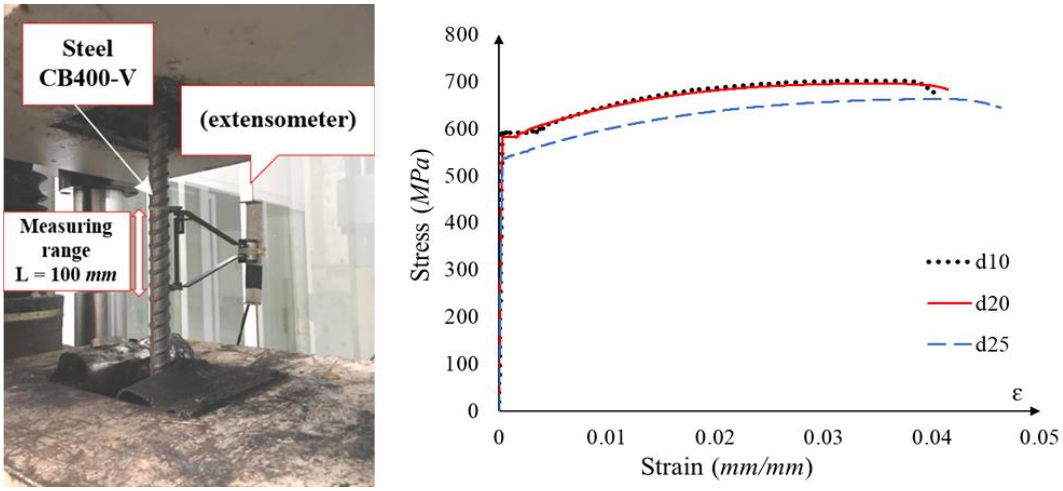

Figure 3. Experimental stress-strain curves of these reinforcements

Conventional concrete with a target compressive strength of 30 MPa was used for non-strengthened regions, while UHPSFRC, with a compressive strength of 150–200 MPa and tensile strength of 8–15.9 MPa, was applied in the strengthened zones of S2 and S3. The UHPSFRC mix included fine aggregates (<2.5 mm), a water-cement ratio of 0.2–0.25, silica fume for particle packing, and 2% volume fraction steel fibers (length 13 mm, diameter 0.2 mm) to enhance ductility and crack resistance. The steel fibers were high-strength, hooked-end fibers with a tensile strength of approximately 1200 MPa, sourced from a commercial supplier (e.g., Bekaert Dramix or equivalent), commonly used in UHPSFRC applications for their superior anchorage and pull-out resistance. The 2% volume fraction (equivalent to 157 kg/m^3) was selected to optimize tensile strength, bond enhancement, and energy dissipation while maintaining workability. These properties were verified through preliminary cube and prism tests, ensuring consistency with UHPSFRC standards [19–23]. The particle size distribution of aggregates is a critical factor in achieving the desired packing density and mechanical performance for both materials. Conventional concrete incorporated a well-graded aggregate mix with particle sizes ranging from 0.075 mm (fine sand) to a maximum of 20 mm (coarse aggregate), following a typical gradation curve for structural concrete. In contrast, UHPSFRC utilized only fine aggregates with sizes ranging from 0.075 mm to 2.5 mm, ensuring a dense matrix through optimized particle packing enhanced by silica fume. This restricted gradation in UHPSFRC contributes to its ultra-high strength and reduced porosity, while the broader gradation in conventional concrete supports workability and cost-effectiveness. Detailed gradation profiles, though not graphically represented, align with standard practices for UHPSFRC and conventional concrete as reported in the literature [19, 23]. For illustrative purposes, approximate cumulative passing percentages for key sieve sizes are summarized in Table 3 to highlight the distinct aggregate characteristics of the two materials.

Table 3. Approximate Particle Size Distribution of Aggregates Used

Sieve Size (mm)	Conventional Concrete (% Passing)	UHPSFRC (% Passing)
20	100	-
10	70–80	-
4.75	50–60	-
2.5	40–50	100
1.18	30–40	70–80
0.6	20–30	50–60
0.3	10–20	30–40
0.075	5–10	10–15

3.4. Specimen Fabrication

The specimens were cast horizontally at a 1:1 scale to replicate real-world construction conditions, using 20 mm thick film-coated wooden formwork sealed with waterproof adhesive to prevent leakage. Aluminum bars with a 50 mm cross-section were employed to reinforce the formwork against casting pressures, ensuring dimensional stability (Figure 4-a). Reinforcement cages were meticulously assembled by fixing longitudinal bars to stirrups using wire ties, with additional transverse bars in the joint region of S1 to maintain stability (Figure 4-b). For S2 and S3, the absence of joint stirrups necessitated careful alignment to ensure UHPSFRC could effectively encase the longitudinal bars.

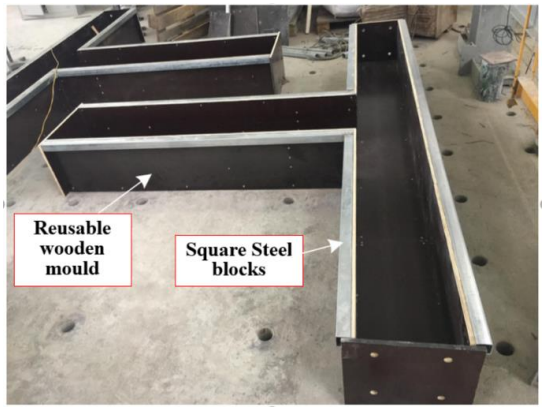

a) Formwork

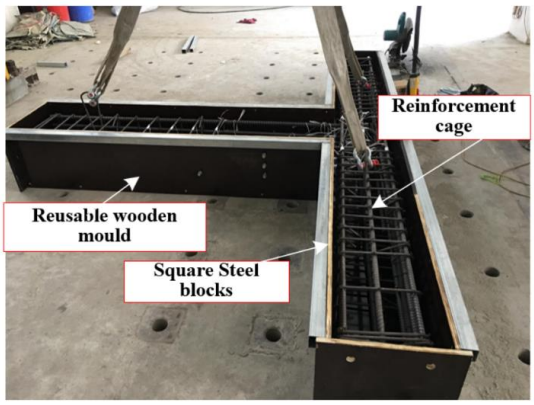

b) Reinforcement cage

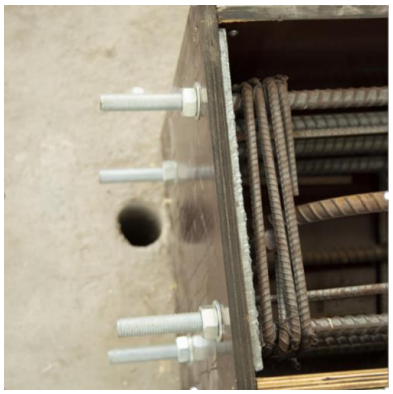

c) Column end details

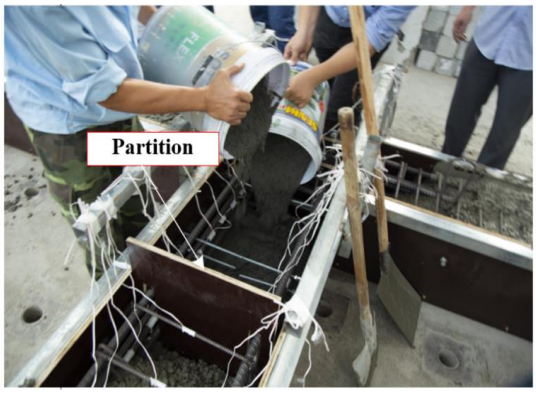

d) Concrete casting

Figure 4. Fabrication process

To facilitate transportation and assembly, lifting hooks made from 25 mm diameter bars were embedded at strategic locations. Spacer blocks maintained a 25 mm concrete cover between reinforcement and formwork. At the column ends, four anchor bolts were secured to steel plates (350 × 350 × 10 mm) to fix loading devices and distribute forces evenly, preventing localized stress concentrations (Figure 4-c). Conventional concrete was mixed at a batch plant and poured into non-strengthened regions, while UHPSFRC was prepared in the laboratory with a 5-minute mixing duration to ensure uniformity. The two concretes were separated by wooden plates during casting, which were removed post-placement to ensure monolithic bonding, followed by thorough vibration (Figure 4-d). After 24 hours, specimens were demolded and cured under wet burlap for 28 days to achieve design strengths (Figure 5). To ensure consistent material properties, curing occurred in a controlled laboratory environment with a temperature maintained at 23 ± 2°C and relative humidity at 95 ± 5%, monitored daily using a digital hygrometer and thermometer. These conditions minimized variations in concrete strength development and UHPSFRC fiber-matrix bonding, aligning with standard practices for high-performance concrete [19, 23].

a) Post-casting curing b) Demolded specimen

Figure 5. Curing Process

3.5. Instrumentation

Before installing instruments, a numerical modelling using ABAQUS was conducted to predict the responses of the frame with the main steps as follows:

- Geometry Development: Three-dimensional finite element (FE) models of specimens S1, S2, and S3 were constructed based on the exact dimensions specified in Table 1 (beam: 350 × 450 mm; column: 350 × 350 mm). Reinforcement details were replicated, and UHPSFRC was modeled as a distinct layer with lengths of 800 mm (S2) and 1025 mm (S3) along the beam and joint region.
- Material Properties Assignment: Conventional concrete was modeled using the Concrete Damaged Plasticity (CDP) model with a compressive strength of 30 MPa and an elastic modulus of 25 GPa. UHPSFRC adopted the CDP model with a compressive strength of 150 MPa, tensile strength of 10 MPa, and strain-hardening behavior derived from experimental data [19]. Steel reinforcement was defined as an elastic-plastic material with yield and ultimate strengths from Table 2 (e.g., fy = 528–585 MPa, fu = 662–701 MPa).
- Boundary Conditions and Loading: The column top was fixed in all degrees of freedom, while an axial load of 650 kN was applied to the column. Cyclic lateral loading was imposed at the beam end following the displacement-controlled protocol used in the experiments, with drift levels ranging from 0% to 6.5%. Perfect bond was assumed between reinforcement and concrete, with an enhanced friction coefficient in UHPSFRC zones to reflect improved interfacial bonding [28].
- Meshing: The model was discretized using 8-node linear brick elements (C3D8R) with reduced integration. Mesh size was set at 25 mm in the joint region for higher resolution of stress concentrations and 50 mm elsewhere to optimize computational efficiency.
- Simulation Execution: Nonlinear static analysis was performed with incremental displacement steps matching the experimental drift levels. Load-displacement responses, crack patterns, and reinforcement strains were extracted at each step.
- Validation: Simulated results were compared with experimental data from Figures 6–12. The model accurately predicted peak loads within a 5–8% error margin (e.g., S1: 185.8 kN experimental vs. 178.5 kN simulated; S2: 220.8 kN vs. 212.3 kN; S3: 231.4 kN vs. 224.6 kN). Crack patterns aligned well with observed X-shaped shear cracks in S1 and beam-dominated cracks in S2, though S3's shear failure was predicted slightly earlier (4.0% drift vs. 6.5% experimental), possibly due to idealized bond assumptions.

To capture crack patterns and reinforcement strain development, each specimen was instrumented with strain gauges (KFG-5-120-A12, 5 mm length, 120 Ω resistance) and linear variable differential transformers (LVDTs). A total of 117 strain gauges were deployed across the three specimens, divided into three groups: 6 gauges on column longitudinal bars near the joint centroid, 25 gauges staggered along top and bottom beam longitudinal bars, and 12 gauges on stirrups in the beam and column (reduced to 37 for S2 and S3 due to absent joint stirrups). Gauge locations were determined from preliminary finite element simulations identifying high-stress zones (Figure 6). LVDTs were placed at key points to measure joint and beam displacements. Data were recorded in real-time using a data logger connected to a computer, ensuring accurate tracking of strain and displacement throughout the loading cycles.

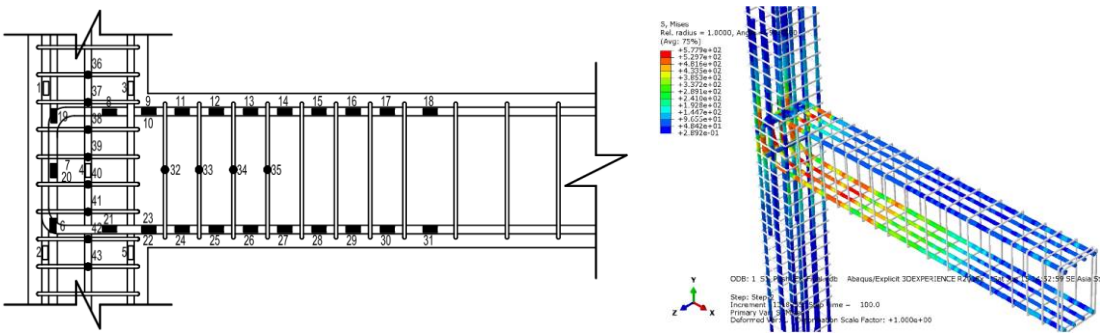

a) S1 with full joint stirrups

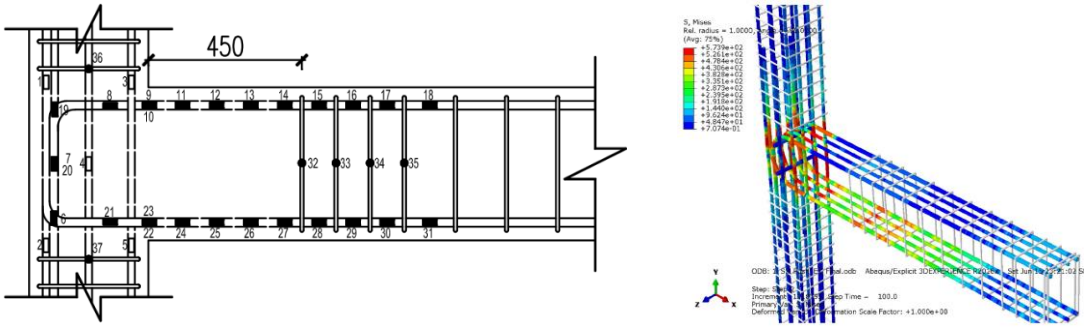

b) S2 with 800 mm UHPSFRC

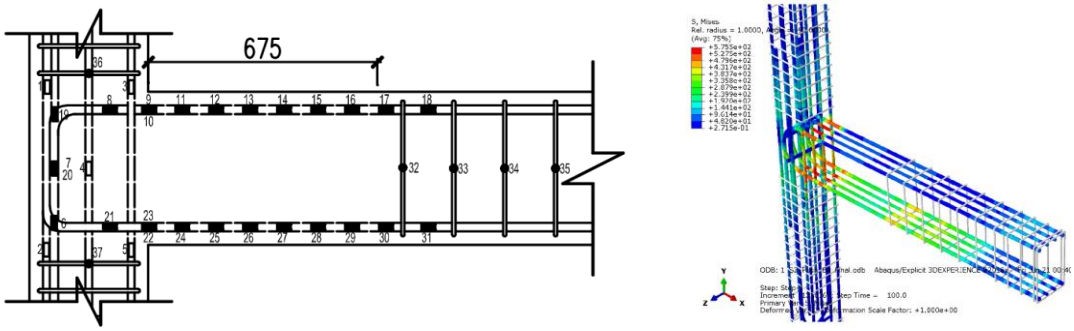

c) S3 with 1025 mm UHPSFRC

Figure 6. Curing Process

4. Experimental Results and Discussion

This section presents a comprehensive analysis of the experimental findings from the cyclic loading tests conducted on three full-scale reinforced concrete (RC) exterior joint specimens: S1 (control), S2 (strengthened with 800 mm UHPSFRC), and S3 (strengthened with 1025 mm UHPSFRC). The investigation focuses on two primary aspects—crack pattern evolution and reinforcement strain development, offering detailed insights into how UHPSFRC influences joint behavior under reversed cyclic loading, with a particular emphasis on its implications for seismic resilience. The results are discussed in terms of failure modes, crack propagation mechanisms, strain distribution, and their broader implications for seismic design and construction practices, providing a deeper understanding of UHPSFRC's role in enhancing structural performance. Comparisons across specimens highlight the role of UHPSFRC strengthening length in altering joint performance, while additional analyses explore unexpected trends, underlying mechanisms, and practical considerations to bridge the gap between experimental observations and real-world applications.

4.1. Crack Patterns

4.1.1. Control Specimen S1

The testing of specimen S1 revealed a classic progression of damage typical of conventionally reinforced RC exterior joints under cyclic loading. During the initial force-controlled phase, the first visible crack emerged at the beam-column interface—a region of high tensile stress concentration due to moment transfer (Figure 7-a). This crack, appearing at a relatively low load (approximately 50–60 kN), marked the onset of joint distress and reflected the inherent weakness of conventional RC joints lacking enhanced confinement, a vulnerability well-documented in seismic failures such as the 1999 Kocaeli earthquake [2]. As the experiment transitioned to displacement control, cracks propagated along the beam length and column ends at drifts of 0.75% and 1.0%, driven primarily by flexural stresses (Figures 7-b and 7-c). These cracks were relatively wide (up to 1 mm at 1.0% drift) and numerous, indicating limited shear resistance and confinement from the stirrups, which struggled to counteract the tensile stresses induced by cyclic loading.

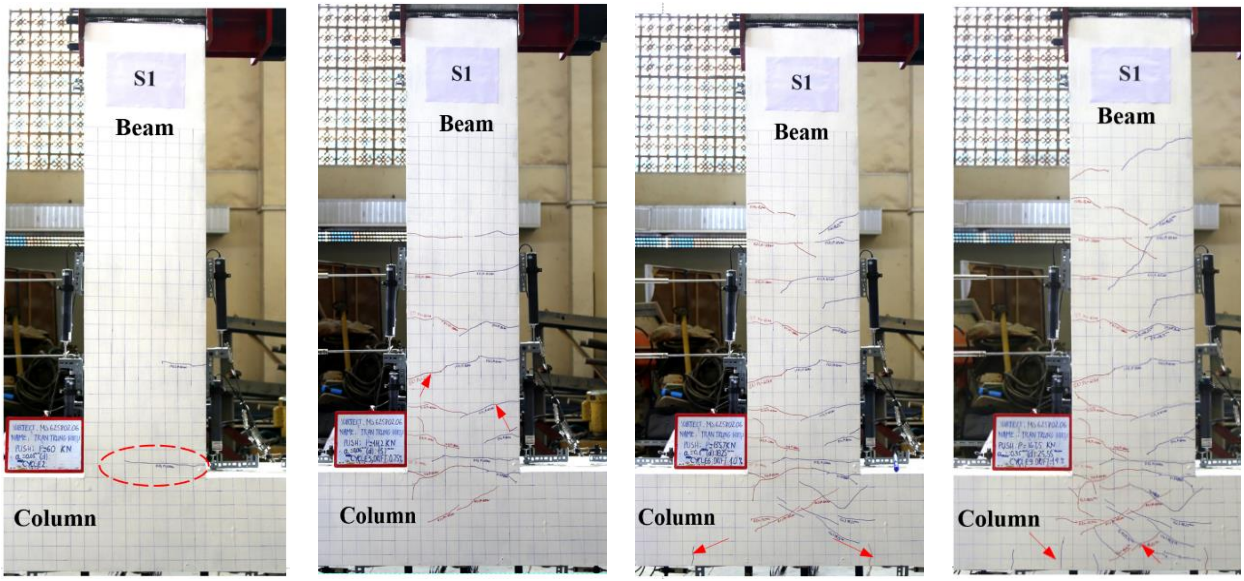

a) First crack b) Drift 0.75% c) Drift 1.0% d) Drift 1.4%

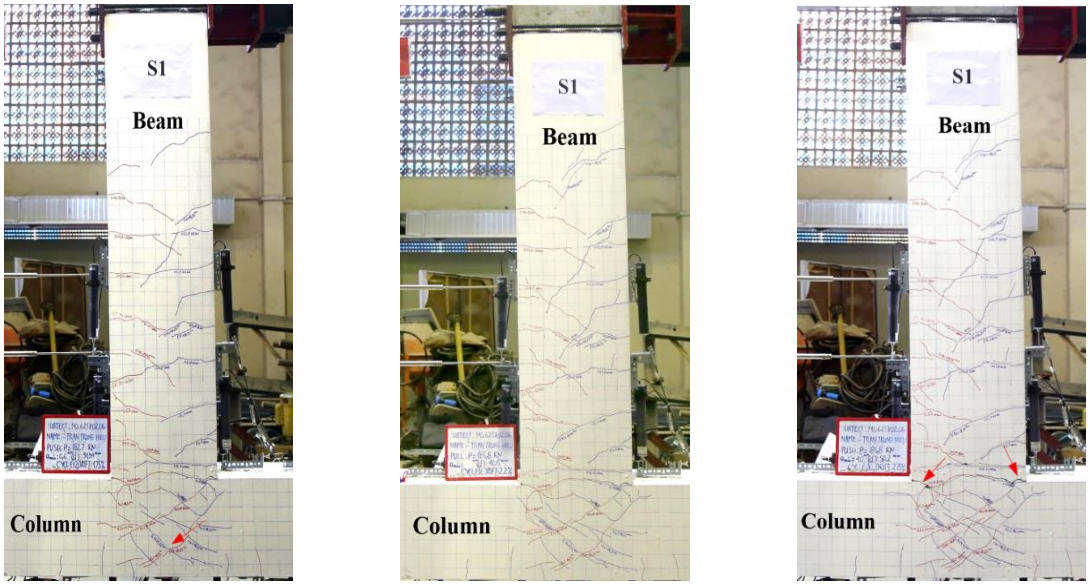

e) Drift 1.75% f) Drift 2.2% g) Drift 2.75%

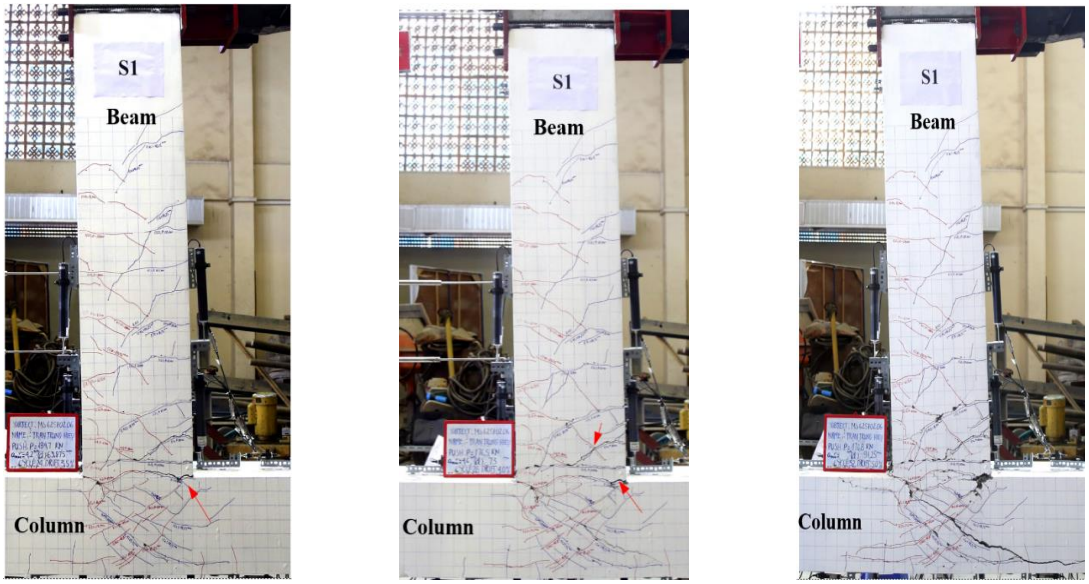

i) Drift 3.5% j) Drift 4.0% k) Drift 5.0%

Figure 7. (a) First crack at beam-column interface, (b) Drift 0.75% showing beam cracking, (c) Drift 1.0% with column end cracks, (d) Drift 1.4% with joint diagonal cracks, (e) Drift 1.75% showing shear distress, (f) Drift 2.2% at peak load with X-shaped pattern.

At 1.4% drift, diagonal cracks formed within the joint, signaling the transition to shear-dominated behavior (Figure 7-d). This development was expected, as exterior joints are particularly susceptible to shear failure due to the lack of a confining beam on one side. The emergence of these diagonal cracks at this drift level highlights the joint's inability to dissipate energy effectively, a common limitation in pre-modern seismic designs where shear capacity relies heavily on concrete alone once tensile cracking initiates. By 1.75% drift, the diagonal crack network intensified, accompanied by initial concrete spalling along the joint edges, indicating significant shear distress (Figure 7-e). This spalling suggests that the six layers of 10 mm stirrups at 80 mm spacing were insufficient to restrain crack growth under increasing cyclic demands, allowing stresses to concentrate and degrade the joint core progressively. At peak load (185.8 kN, 2.2% drift), a pronounced X-shaped crack pattern fully developed across the joint core, extending approximately 50 mm into the column's back face (Figure 7-f). This pattern is characteristic of shear failure in RC joints, where diagonal tension exceeds the concrete's capacity, and transverse reinforcement struggles to restrain crack widening. The crack widths at this stage reached 1.5–2 mm, reflecting a significant loss of structural integrity and exposing the joint's brittle nature under cyclic loading, a failure mode that compromises energy dissipation and increases collapse risk in seismic events.

As drift increased to 2.75%, crack widths grew substantially, with some exceeding 2 mm, and additional spalling occurred along the beam-column interface (Figure 7-g). This escalation underscores the progressive loss of confinement as the concrete core fractured, allowing cracks to propagate freely and highlighting the inadequacy of conventional detailing in sustaining repeated load reversals. Severe damage became evident at 3.5% drift, marked by extensive diagonal crack propagation, widespread concrete spalling, and visible rebar exposure at multiple locations within the joint (Figure 7-i). This stage highlighted the limitations of conventional reinforcement in resisting cyclic shear, as the concrete core disintegrated under repeated loading. At 4.0% drift, under reversed loading cycles, cracks widened further—some reaching 5 mm—and the concrete cover detached from the beam, exacerbating joint degradation (Figure 7-j). The experiment concluded at 5.0% drift with complete joint failure, characterized by concrete crushing, longitudinal rebar rupture, and a collapsed joint core (Figure 7-k). This shear-dominated failure aligns closely with Tuken et al. [1], who observed similar X-shaped crack patterns and peak loads (around 180–190 kN) in conventionally reinforced RC joints under cyclic loading, attributing failure to inadequate shear capacity and poor confinement. However, unlike their study, which used UHPC jacketing to achieve a 20–30% load increase, S1 serves as a baseline without retrofitting, confirming the vulnerability of standard joints and setting the stage for UHPSFRC's comparative benefits.

4.1.2. Strengthened Specimen S2

Specimen S2, strengthened with an 800 mm UHPSFRC layer, exhibited a markedly different crack evolution compared to S1, reflecting the material's superior tensile and confinement properties. The first crack appeared during the force-controlled phase ($P \leq 80$ kN) at the interface between UHPSFRC and conventional concrete, located 450 mm from the column face (Figure 8-a). This position, corresponding to the end of the strengthened zone, suggests a stress discontinuity due to the transition in material properties, with UHPSFRC's higher stiffness contrasting with the weaker conventional concrete. Unlike S1's wider initial crack (approximately 0.5–1 mm), this crack was notably narrower (approximately 0.2 mm), likely due to the crack-bridging effect of steel fibers in UHPSFRC, which distribute tensile stresses across multiple micro-cracks rather than allowing localized widening—a mechanism that enhances early-stage damage tolerance [19].

During the displacement-controlled phase, cracks distributed uniformly along the beam at 0.75% and 1.0% drifts, similar to S1 in pattern but significantly reduced in width and number (Figures 8-b and 8-c). These cracks, ranging from 0.1–0.3 mm, indicate that UHPSFRC's high tensile strength (8–15.9 MPa) and fiber reinforcement effectively controlled crack initiation and propagation, allowing the joint to sustain cyclic loads with minimal distress compared to S1's wider cracks (up to 1 mm). This finer crack network suggests improved energy dissipation capacity, a critical factor for seismic performance. Notably, at 1.4% drift, no cracks appeared in the column—a stark contrast to S1—indicating that UHPSFRC effectively confined the joint core and redistributed stresses away from the column (Figure 8-d). Diagonal cracks emerged in the joint at 1.75% drift, mirroring S1's shear pattern but remaining finer and less extensive, with maximum widths below 0.5 mm (Figure 8-e). This suggests that UHPSFRC not only delayed crack initiation but also controlled their propagation, a critical advantage for seismic performance. The delayed onset and reduced severity of these cracks highlight UHPSFRC's enhanced shear resistance, likely due to its dense matrix (low porosity from a 0.2–0.25 water-cement ratio) and improved fiber-matrix bonding, which collectively mitigate tensile failure under cyclic shear [5].

At peak load (220.8 kN, 2.2% drift), a distinct failure pattern emerged: curved cracks extended 150 mm into the column's back face, accompanied by horizontal cracks along the beam, indicating a shift toward beam-dominated flexural failure rather than joint shear failure (Figure 8-f). This 19% increase in peak load over S1 (185.8 kN) reflects UHPSFRC's significant contribution to shear capacity, achieved by replacing transverse reinforcement with a material that provides both strength and confinement. The curved crack pattern suggests that UHPSFRC redistributed bending stresses, allowing the beam to yield plastically before the joint failed—a desirable outcome in seismic design that enhances ductility and prevents brittle collapse. This beam flexural failure mode, characterized by progressive yielding

and concrete crushing in the beam beyond the strengthened zone (observed at 4.0% drift, Figure 8i), contrasts sharply with S1's brittle shear collapse. The shift to flexural failure enabled S2 to absorb and dissipate seismic energy through plastic deformation over a larger drift range (up to 6.5%), as evidenced by sustained strain growth to 8000 μm/m, improving seismic performance by delaying catastrophic joint failure and enhancing overall frame stability. This observation aligns with the intended design goal of relocating damage outside the joint, leveraging UHPSFRC's enhanced tensile capacity. At 2.75% drift, a prominent curved crack reached two-thirds of the beam depth (approximately 300 mm), yet the joint core remained largely intact, with minimal spalling (Figure 8-g). By 3.5% drift, damage stabilized within the joint, with no significant deterioration beyond the beam's strengthened zone (Figure 8-h). The confinement provided by UHPSFRC's steel fibers (2% volume fraction) likely contributed to this controlled damage progression, limiting crack widening and spalling even at higher drifts.

From 4.0% to 6.5% drift, failure progressively concentrated in the beam, with concrete crushing observed at 4.0% drift (Figure 8-i) and longitudinal rebar rupture at 6.5% drift (Figure 8-k). Unlike S1's abrupt joint collapse, S2's failure was gradual, with damage confined to the beam beyond the UHPSFRC region (Figure 8-j). This shift to flexural failure and 19% load increase (220.8 kN vs. 185.8 kN) aligns with Kubair & Kalyana Rama [9], who reported a 15–25% capacity increase in UHPSFRC-strengthened RC joints under high axial loads, achieving peak loads of 210–230 kN with a similar transition to beam failure. However, Kubair & Kalyana Rama et al. [9] noted wider cracks (0.8–1.2 mm) at peak load, suggesting that the 2% steel fiber content in this study's UHPSFRC mix provided superior crack control compared to their 1.5% fiber volume. Additionally, Ghasemi et al. [31] observed a comparable shift to beam failure with UHPSFRC strengthening, though their peak loads (200–215 kN) were slightly lower, possibly due to differences in joint geometry or axial load (500 kN vs. 650 kN here). The finer cracks and higher ductility in S2 indicate that the 800 mm length optimizes UHPSFRC's confinement and tensile benefits, surpassing previous studies in crack width reduction.

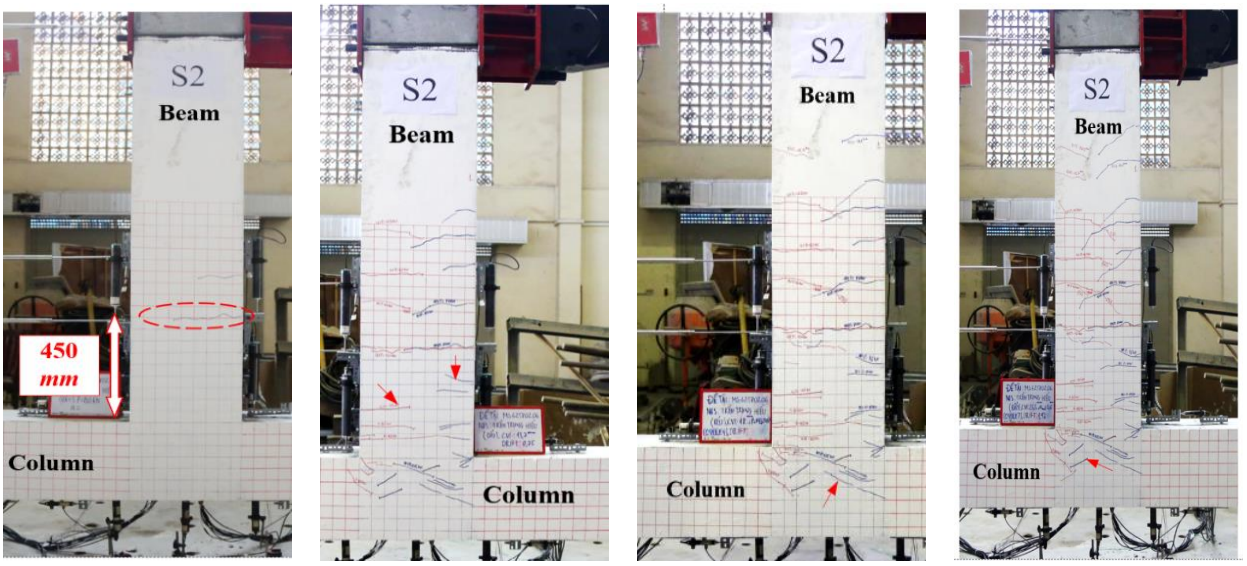

a) First crack b) Drift 0.75% c) Drift 1.0% d) Drift 1.4%

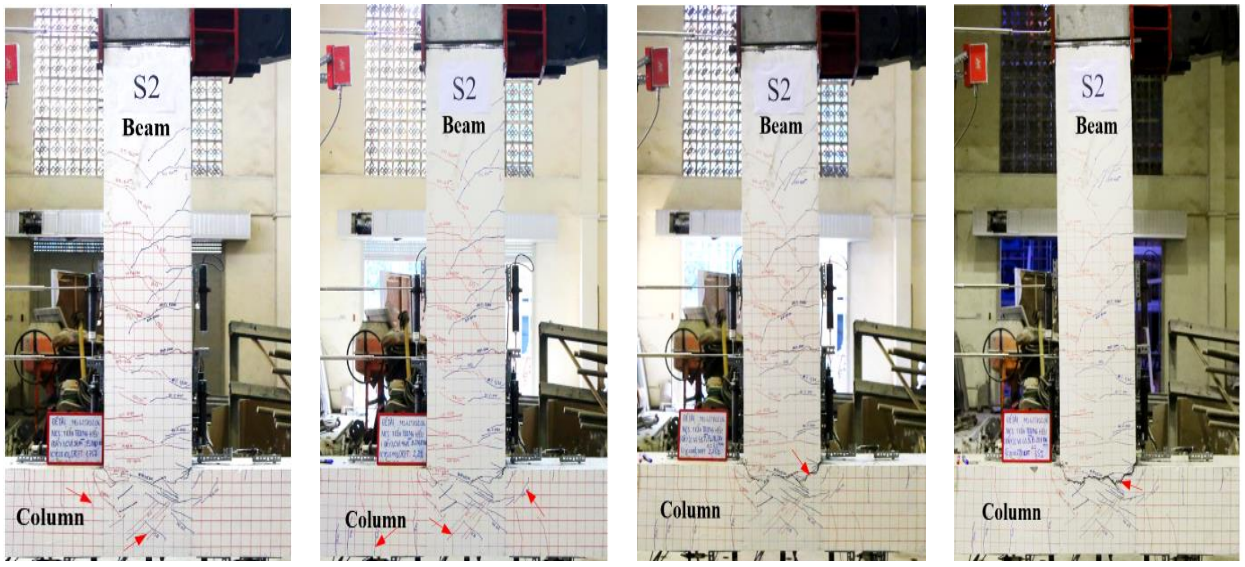

e) Drift 1.75% f) Drift 2.2% g) Drift 2.75% h) Drift 3.5%

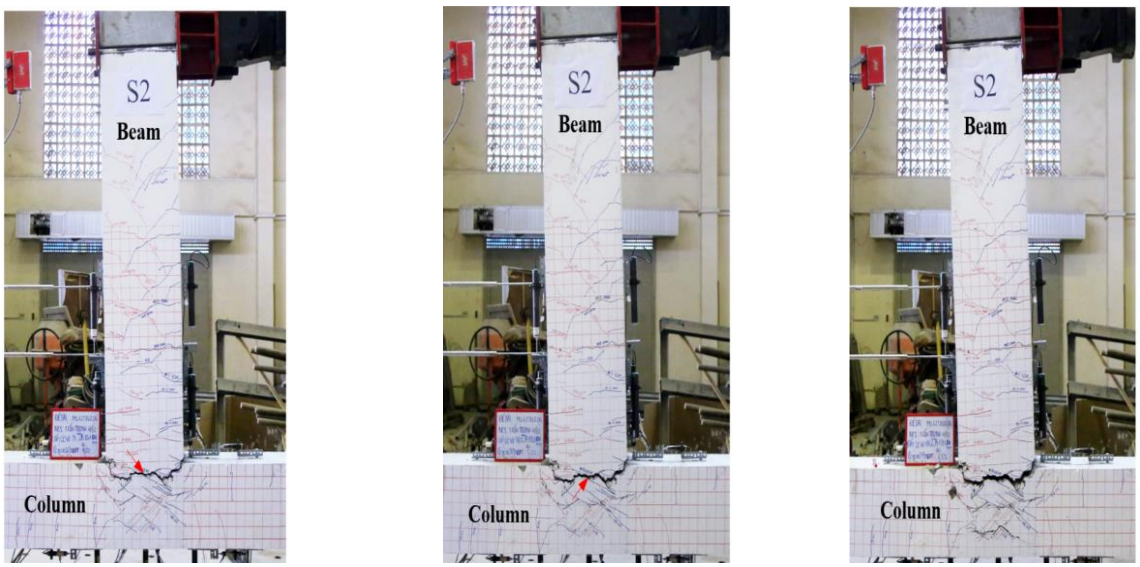

i) Drift 4.0% j) Drift 5.0% k) Drift 6.5%

Figure 8. (a) First crack at material interface, (b) Drift 0.75% with beam cracks, (c) Drift 1.0% showing uniform distribution, (d) Drift 1.4% without column cracks, (e) Drift 1.75% with diagonal cracks, (f) Drift 2.2% at peak load with curved cracks, (g) Drift 2.75% with extended beam cracks, (h) Drift 3.5% with stable joint, (i) Drift 4.0% with beam damage, (j) Drift 5.0% with progressive failure, (k) Drift 6.5% with rebar rupture.

4.1.3. Strengthened Specimen S3

Specimen S3, with a 1025 mm UHPSFRC strengthening length, shared similarities with S2 but diverged in its ultimate failure mode, illustrating the nuanced impact of strengthening extent. The initial crack appeared during the force-controlled phase ($P \leq 80$ kN) at the UHPSFRC-concrete interface, 675 mm from the column face, reflecting a similar material transition effect as S2 (Figure 9-a). This crack, though fine (approximately 0.3 mm), was positioned further from the joint, suggesting that the extended UHPSFRC length redistributed initial stresses along a broader beam segment. During displacement control, cracks spread evenly along the beam at 0.75% and 1.0% drifts, maintaining narrow widths (<0.5 mm) due to UHPSFRC's fiber reinforcement (Figures 9-b and 9-c). This controlled crack distribution mirrors S2 but extends further, indicating that the longer UHPSFRC layer enhanced tensile resistance across a larger area, though it may have shifted critical stresses closer to the joint core as loading intensified.

At 1.4% drift, S3 mirrored S2's behavior with no column cracks, reinforcing the effectiveness of UHPSFRC in joint confinement (Figure 9-d). However, at 1.75% drift, X-shaped diagonal cracks emerged in the joint core, similar to S1 but less severe, with widths limited to 0.7 mm (Figure 9-e). At peak load (231.4 kN, 2.2% drift), cracks extended 150 mm into the column's back face, accompanied by additional diagonal and horizontal cracks, indicating a mixed failure mode (Figure 9-f). This 25% higher peak load compared to S1 (185.8 kN) and 5% higher than S2 (220.8 kN) demonstrates that the longer UHPSFRC length further enhanced capacity, likely by distributing shear stresses over a larger reinforced area. However, the mixed failure mode hints at a trade-off between strength and ductility, warranting further investigation into optimal strengthening lengths.

At 2.75% drift, a curved crack formed at the beam-column intersection, 50 mm from the column face, reaching significant depth (approximately 250 mm), while diagonal cracks in the joint widened slightly (Figure 9g). Severe damage became apparent at 3.5% drift, with cracks perpendicular to the column axis, concrete spalling in the joint core, and propagation into the column reaching 150 mm (Figure 9-h). The increased severity compared to S2 indicates that the 1025 mm length may have over-strengthened the beam, reducing its flexibility and forcing the joint to absorb more energy, a reversal from S2's beam-dominated failure. From 4.0% to 5.0% drift, extensive diagonal cracking covered the joint, with widths exceeding 2 mm, and further column damage emerged (Figures 9-j and 9-j). The experiment concluded at 6.5% drift with complete joint concrete crushing and significant rebar exposure (Figure 9-k). This shear-dominated failure mode, though delayed and less brittle than S1's due to UHPSFRC's confinement (crack widths 0.7–2 mm vs. >2 mm in S1), indicates that the 1025 mm length over-strengthened the beam, shifting critical stresses back to the joint. Unlike S2, S3's failure involved rapid joint degradation after peak load, limiting ductility (strain dropped to 8500 µm/m by 5.0% drift, yet its higher capacity and finer initial cracks still offered improved energy dissipation compared to S1's abrupt collapse, contributing to seismic performance by delaying failure progression.

This reversion to shear failure despite a 25% load increase over S1 contrasts with Yoo et al. [3], who achieved consistent beam failure in UHPSFRC-jacketed bridge piers with peak loads of 220–240 kN, using a shorter jacket length (600–700 mm). Their study maintained crack widths below 0.6 mm, similar to S3's early stages, but avoided shear failure, possibly due to lower axial loads (300–400 kN vs. 650 kN here) or thicker jackets (50 mm vs. 25 mm cover in this study). Conversely, Valcuende et al. [27] reported shear failure in UHPSFRC-strengthened elements under seismic loading, with peak loads around 230 kN and crack widths up to 1 mm, aligning with S3's outcome but with less ductility.

The higher capacity in S3 compared to S2 and previous studies suggests that the 1025 mm length maximized strength but over-stiffened the beam, redirecting stresses to the joint, a trend not observed in S2 or Yoo et al.'s [3] shorter configurations. This comparison highlights a critical threshold in UHPSFRC application length, beyond which ductility diminishes, offering a nuanced advancement over prior work.

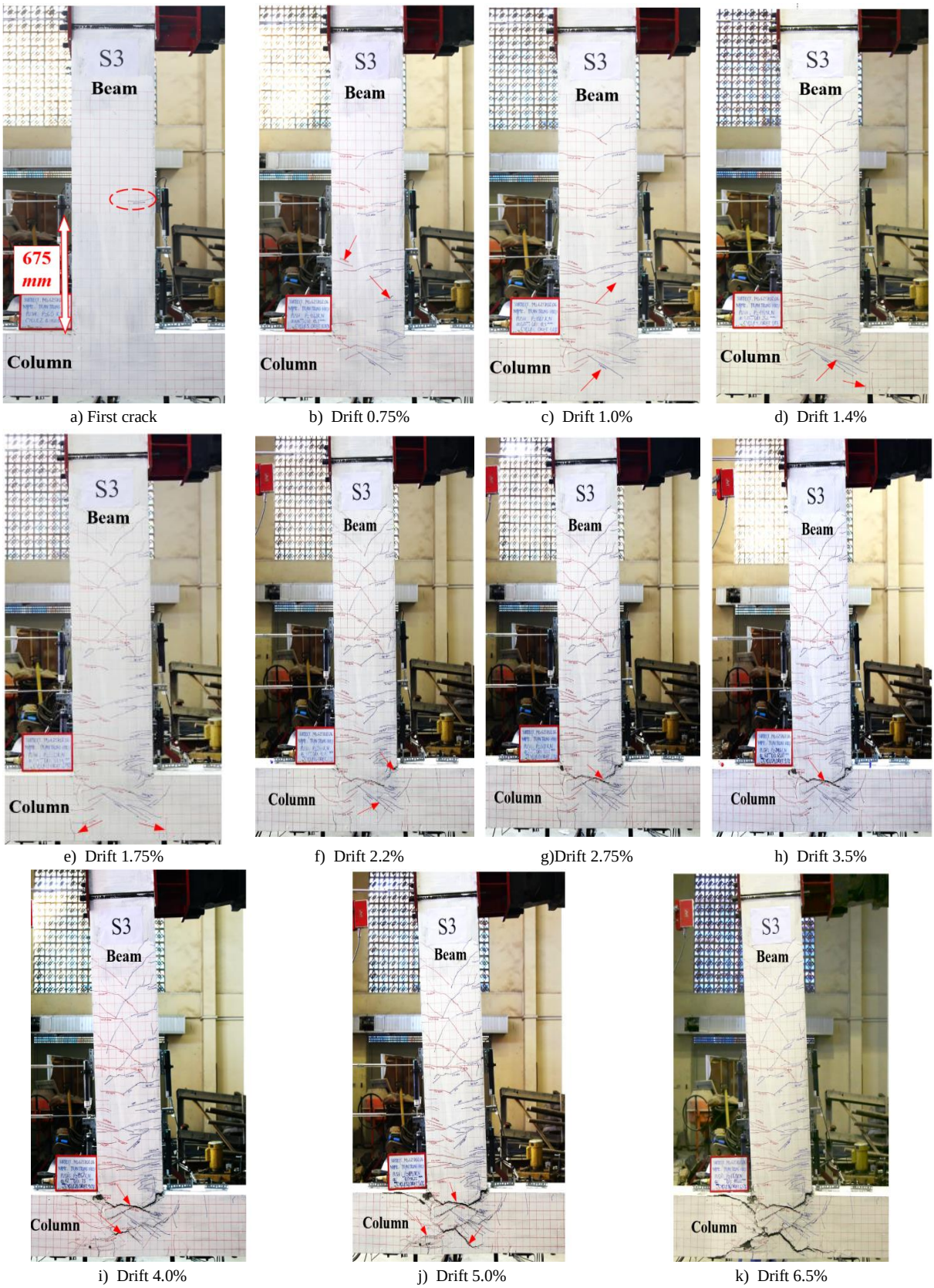

a) First crack b) Drift 0.75% c) Drift 1.0% d) Drift 1.4%

e) Drift 1.75% f) Drift 2.2% g)Drift 2.75% h) Drift 3.5%

i) Drift 4.0% j) Drift 5.0% k) Drift 6.5%

Figure 9. (a) First crack at interface, (b) Drift 0.75% with beam cracks, (c) Drift 1.0% showing distribution, (d) Drift 1.4% without column cracks, (e) Drift 1.75% with X-shaped cracks, (f) Drift 2.2% at peak load with extended cracks, (g) Drift 2.75% with curved crack, (h) Drift 3.5% with joint damage, (i) Drift 4.0% with widespread cracking, (j) Drift 5.0% with intensified damage, (k) Drift 6.5% with joint failure.

4.2. Reinforcement Strain Development

The reinforcement strain development in the control specimen (S1) and the UHPSFRC-strengthened specimens (S2 and S3) was systematically compared to evaluate the impact of UHPSFRC on joint behavior under reversed cyclic loading. Strain gauges positioned along the longitudinal bars of the beam and column, as well as beam stirrups (Figure 6), provided a detailed picture of strain evolution, captured in real-time via a data logger at a sampling rate of 10 Hz. The comparison focused on three key criteria: (1) the onset of yielding, defined as the drift level where strain exceeded the yield threshold (2800 µm/m, based on the steel's yield strength of 528–585 MPa from Table 2); (2) peak strain at maximum load (2.2% drift), indicating the maximum tensile demand on reinforcement; and (3) post-peak strain behavior up to failure (5.0% for S1, 6.5% for S2 and S3), reflecting ductility and damage progression. These criteria were selected to quantify how UHPSFRC alters strain distribution, plastic hinge formation, and energy dissipation compared to conventional reinforcement, providing insights into seismic performance enhancement.

4.2.1. Longitudinal Reinforcement in Beam

Strain gauges positioned along the top and bottom longitudinal bars of the beam (Figure 6) provided a detailed picture of strain evolution, captured in real-time via a data logger. For S1 and S2, yielding occurred at 1.4% drift, with strains of 2798 µm/m and 2678 µm/m, respectively, indicating the onset of plastic deformation (Figure 10). S3, however, reached yield earlier at 1.0% drift, peaking at 4744 µm/m by 1.4% drift, reflecting a more rapid strain accumulation possibly due to the extended UHPSFRC length altering stress distribution (Figure 10). This earlier yielding in S3 compared to S1 and S2 highlights UHPSFRC's influence in accelerating tensile demands near the joint, likely due to increased stiffness from the 1025 mm strengthened zone. At peak load (2.2% drift), strains escalated to 9873 µm/m (S1), 5498 µm/m (S2), and 11972 µm/m (S3), with S3 exhibiting a 30% higher strain than S1 and over twice that of S2 (Figure 11). The significantly lower peak strain in S2 compared to S1 and S3 demonstrates UHPSFRC's ability to redistribute stresses away from the joint core at the 800 mm length, while S3's higher strain suggests over-strengthening intensified local demands, contributing to its shear failure mode.

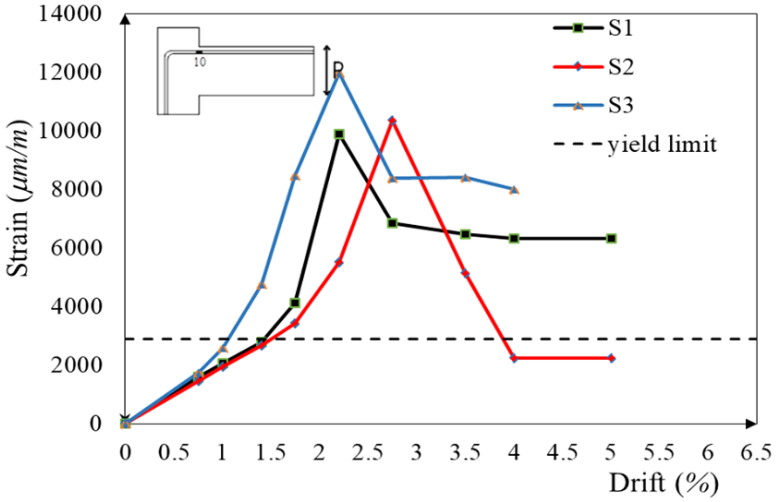

Figure 10. Strain at Gauge #10 across specimens

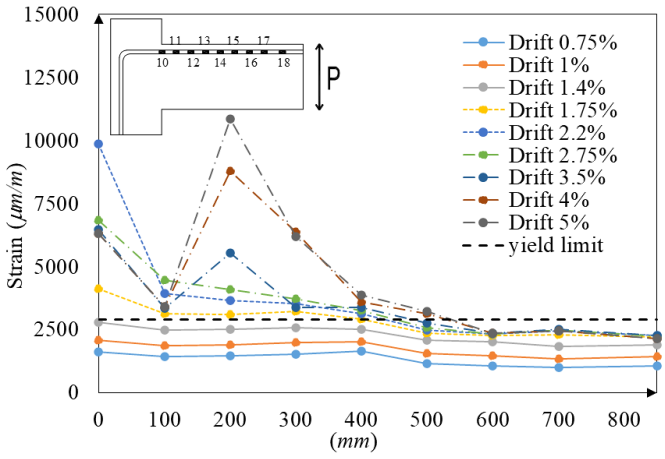

a) S1 with peak at 200 mm

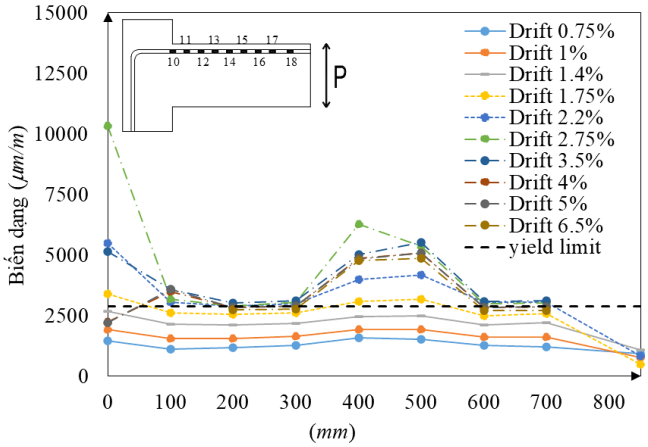

b) S2 with peak at 400–500 mm

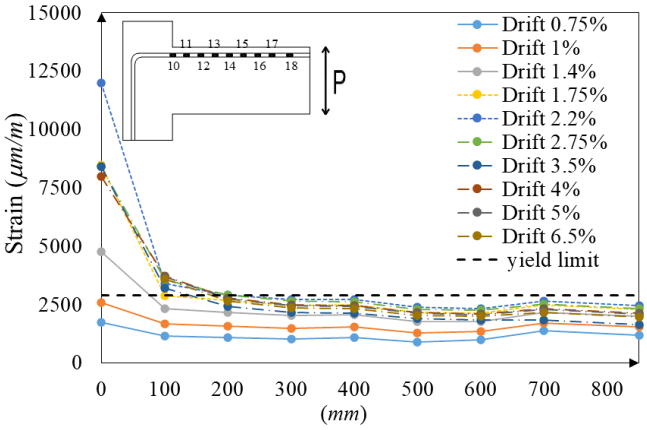

c) S3 with early yielding and high strain

Figure 11. Drift-strain relationship for beam longitudinal reinforcement

Post-peak behavior further differentiated the specimens. S1 and S3 showed a decline in strain after 2.2% drift, with values dropping to 7000 µm/m and 8500 µm/m by 5.0% drift, respectively, indicating damage localization and reduced load-carrying capacity (Figures 11-a and 11-c). Conversely, S2's strain continued to rise, reaching 8000 µm/m by 6.5% drift, demonstrating sustained ductility and a gradual failure progression (Figure 11-b). This sustained strain increase in S2, unlike the decline in S1 and S3, underscores UHPSFRC's enhancement of ductility at the optimal 800 mm length, allowing progressive energy dissipation through beam yielding rather than abrupt joint collapse. The strain distribution revealed distinct plastic hinge locations: S1's maximum strain occurred at Gauge #12 (200 mm from the column), outside the joint, consistent with shear failure shifting damage to the beam-column interface. S2's peak strain was at Gauges #14–15 (400–500 mm), aligning with the UHPSFRC boundary, effectively relocating the hinge away from the joint and supporting its beam failure mode. S3's early yielding and high peak strain at Gauge #10 (near the joint) suggest a less controlled hinge formation, potentially due to insufficient confinement beyond 1025 mm, correlating with its joint shear failure. These strain profiles align with Shao et al. [28], who reported peak strains of 5000–6000 µm/m in UHPSFRC-strengthened beams under cyclic loading, with a gradual increase similar to S2, though their study maintained lower maximum strains (7000 µm/m) due to a shorter strengthened length (600 mm). In contrast, Huang et al. [15] observed higher peak strains (10,000–12,000 µm/m) in UHPSFRC with embedded reinforcement, matching S3's values but without the subsequent decline, suggesting that S3's extended length intensified strain concentration near the joint, contributing to shear failure. The lower peak strain in S2 compared to both S3 and Huang et al. [15] indicates an optimal balance of capacity and ductility, advancing beyond previous studies by achieving controlled hinge relocation.

4.2.2. Longitudinal Reinforcement in Column

Column longitudinal strains, measured near the joint centroid (Figure 6), remained well below yield (<2800 µm/m) due to the combined effects of a 650 kN axial load and lateral cyclic loading. At peak load (2.2% drift), strains were 1262 µm/m (S1), 1471 µm/m (S2), and 1572 µm/m (S3), with S3 exhibiting the highest value (Figure 12). This comparison reveals that UHPSFRC in S2 and S3 increased column strains by 16–25% over S1, reflecting greater joint distress in S3 and balanced load transfer in S2, though all remained elastic due to axial confinement. This trend reflects S3's greater joint distress, where diagonal cracking amplified tensile stresses at the column-joint interface, whereas S2's balanced confinement minimized such effects. This trend persisted throughout the test, with S3 reaching 1800 µm/m at

6.5% drift, compared to 1500 µm/m (S2) and 1400 µm/m (S1). The elevated strain in S3 correlates with its extensive joint cracking, which amplified tensile stresses at the column-joint interface as diagonal cracks propagated into the column face. The elevated strain in S3 correlates with its extensive joint cracking, suggesting that the longer UHPSFRC length inadvertently increased column reinforcement demands, a potential concern in real structures with variable axial loads.

S2's intermediate strain suggests a balanced load transfer, with UHPSFRC mitigating shear-induced tensile demands on the column reinforcement. S1's lower strain reflects typical behavior in conventionally reinforced joints, where damage concentrates in the joint core rather than the column. Zainal et al. [8] reported similar column strains (1200–1500 µm/m) in high-strength concrete joints with hybrid fibers, though their study achieved yielding at higher drifts (3.0%) due to additional transverse reinforcement, unlike S1–S3, where joint failure preceded column yielding. The higher strain in S3 compared to S2 and Zainal et al. [8] suggests that the 1025 mm UHPSFRC length increased column demands, a finding not emphasized in prior work, highlighting the need for integrated beam-column design when extending strengthening lengths.

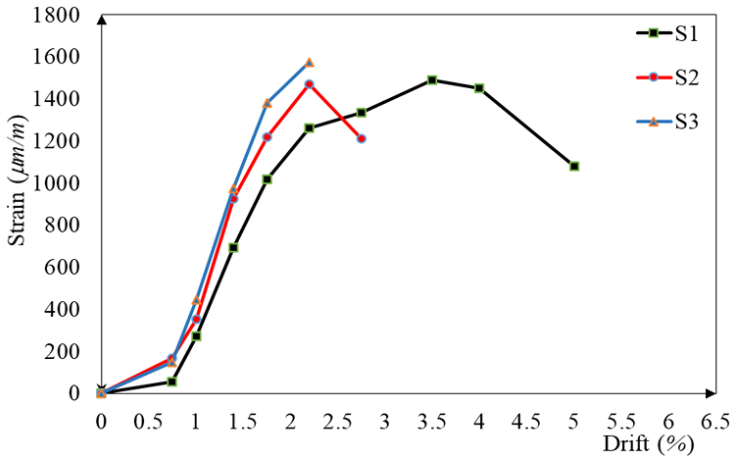

Figure 12. Drift-strain relationship for column longitudinal reinforcement

4.2.3. Stirrups in Beam

Beam stirrup strains, monitored at four locations near the joint (Figure 6), remained below the yield threshold (<2800 µm/m) across all specimens, reflecting their secondary role in shear resistance under UHPSFRC strengthening (Figure 12). S1's strains grew steadily, peaking at 2500 µm/m at 5.0% drift, consistent with conventional confinement behavior (Figure 13-a). S2 and S3, lacking joint stirrups, showed higher strains at Gauge #34 (near the joint), reaching 2700 µm/m at 6.5% drift (S2) and 2600 µm/m at 2.2% drift (S3), then declining in S3 (Figures 13-b and 13-c). Compared to S1, S2's higher sustained strain indicates UHPSFRC effectively replaced stirrup confinement, while S3's early peak and decline suggest strain concentration shifted to the joint, consistent with its shear failure. Li et al. [19] observed lower stirrup strains (2000–2200 µm/m) in UHPSFRC with low fiber content under dynamic loading, attributing this to fiber confinement, though their study included stirrups throughout, unlike S2 and S3. The near-yield strains in S2 and S3 demonstrate UHPSFRC's ability to replace stirrups effectively, a finding that extends beyond Li et al. [19] by eliminating transverse reinforcement entirely while maintaining shear resistance, offering a practical simplification for seismic retrofitting.

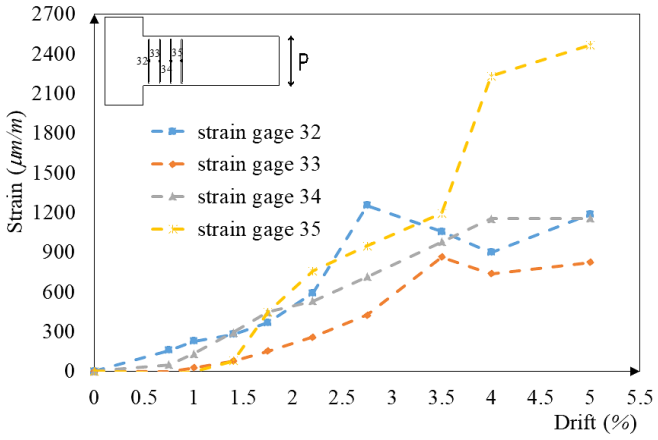

a) S1 with steady growth

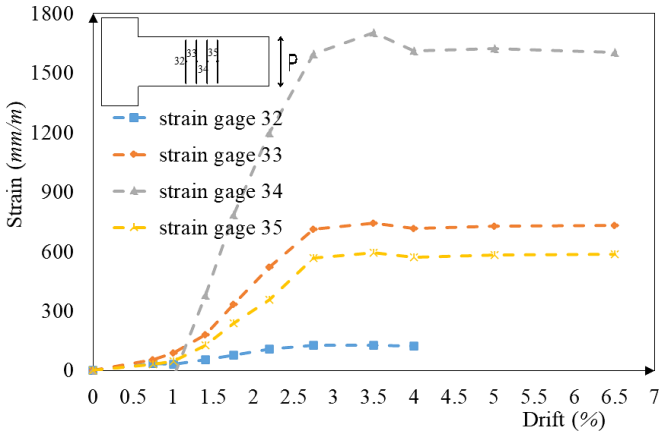

b) S2 with sustained development

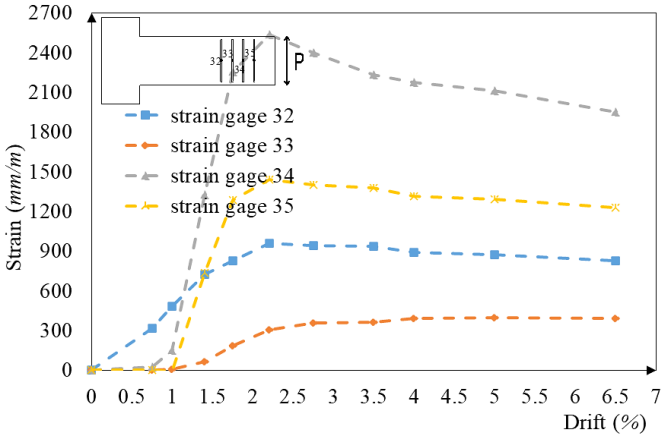

c) S3 with peak and decline

Figure 13. Drift-strain relationship for beam stirrups

4.3. Discussion

The crack patterns and strain data reveal a complex interplay between UHPSFRC strengthening length and joint performance. S1's shear failure underscores the limitations of conventional reinforcement in resisting cyclic loading, with wide cracks and rapid joint degradation reflecting inadequate confinement. The narrower crack widths observed in S2 and S3 (<0.5 mm vs. >2 mm in S1) highlight UHPSFRC's crack control, attributed to steel fiber bridging and improved bond strength, which could reduce long-term deterioration (e.g., corrosion) in seismic regions. This aligns with findings by Li et al. [19], who noted that UHPSFRC's strain-hardening behavior under dynamic loading significantly mitigates crack widening, enhancing long-term durability in seismic applications.

S2's transition to beam flexural failure, with a 19% increase in peak load (220.8 kN vs. 185.8 kN), demonstrates UHPSFRC's ability to enhance shear capacity and relocate damage, offering a practical solution for seismic retrofitting where joint access is limited. The sustained strain growth in S2, as opposed to the decline in S1 and S3, corroborates Li et al. [19], who found that hybrid fiber reinforcement in high-strength concrete joints enhances ductility by redistributing strains away from the joint core. Conversely, S3's higher capacity (231.4 kN) but reversion to shear failure suggests an optimal strengthening length exists—around 800 mm in this study—beyond which benefits diminish, potentially due to over-strengthening the beam and under-protecting the joint. The shift from shear failure in S3 to flexural failure in S2 supports Ghasemi et al. [31], who demonstrated that UHPSFRC strengthening length critically influences failure modes, with optimal lengths preventing joint shear collapse under cyclic loads.

Strain development comparisons between S1 and the UHPSFRC specimens (S2, S3) reveal distinct performance enhancements. S1 exhibited high peak strains (9873 µm/m) and rapid post-peak decline, indicative of brittle shear failure and limited ductility. In contrast, S2's lower peak strain (5498 µm/m) and sustained increase to 8000 µm/m reflect improved ductility and controlled hinge relocation, driven by UHPSFRC's confinement and fiber bonding. S3's excessive peak strain (11972 µm/m) and subsequent drop highlight a trade-off between capacity and ductility at longer strengthening lengths. These differences, measured via yielding onset, peak strain, and post-peak behavior, underscore UHPSFRC's role in optimizing strain distribution for seismic resilience, with S2 achieving the best balance.

The 800 mm strengthening length in S2 proved optimal due to its ability to balance beam stiffness and joint confinement, effectively relocating the plastic hinge to the beam while maintaining joint integrity. This length,

approximately twice the beam depth (450 mm), aligns with the effective plastic hinge zone (typically 1–2 times the member depth) where flexural yielding is desired in seismic design, as per FEMA 356 guidelines. By strengthening up to 800 mm, UHPSFRC enhanced the beam's tensile capacity and shear resistance sufficiently to induce yielding beyond the joint, as evidenced by curved cracks extending 150 mm into the column's back face and peak strains shifting to 400–500 mm from the column (Gauges #14–15). In contrast, S3's 1025 mm length—over 2.2 times the beam depth—over-stiffened the beam, reducing its flexibility and forcing shear stresses back into the joint core, as shown by X-shaped cracks and higher strains near the joint (Gauge #10). This suggests that beyond a critical length (approximately 800 mm here), additional UHPSFRC amplifies beam rigidity without proportionally enhancing joint confinement, leading to shear failure despite a 25% capacity increase (231.4 kN vs. 185.8 kN in S1). The length of UHPSFRC application thus directly influenced both failure mode—shifting from shear in S1 and S3 to flexural in S2—and ultimate load-carrying capacity, with S2's 19% increase reflecting efficient stress redistribution and S3's 25% increase indicating strength gains at the expense of ductility. Preliminary ABAQUS simulations corroborated this, predicting beam hinge formation at 800 mm and joint shear distress at 1025 mm, validating the experimental trends.

The failure modes of UHPSFRC-strengthened specimens—flexural in S2 and shear in S3—differ markedly from S1's shear-dominated failure, enhancing seismic performance in distinct ways. S2's beam flexural failure allowed ductile yielding and energy dissipation through plastic hinge formation, as seen in sustained strain growth and a 19% capacity increase, aligning with seismic design goals of controlled damage and collapse prevention. S3's shear failure, though less brittle than S1's due to UHPSFRC's confinement (delayed to 6.5% drift vs. 5.0% in S1), still limited ductility, yet its 25% higher capacity and finer cracks improved energy absorption compared to S1, reducing the risk of sudden collapse. These differences highlight UHPSFRC's potential to tailor failure modes for seismic resilience, with S2 optimizing ductility and S3 maximizing strength, both surpassing S1's brittle response.

The practical implications of tailoring UHPSFRC length, as seen in S2's optimal performance, are reinforced by Xiong et al. [32], who found that UHPC connections in precast joints improve construction efficiency and seismic resilience by optimizing damage distribution. This suggests that UHPSFRC can address construction challenges by replacing stirrups in congested joint regions, improving concrete placement and structural resilience. However, the variability in failure modes emphasizes the importance of calibrating strengthening length to specific joint geometries and loading conditions. Tuken et al. [1] further support this, reporting that UHPC jacketing significantly reduces crack propagation in RC joints under cyclic loading, enhancing damage tolerance, which is evident in S2 and S3's finer crack networks compared to S1.

An unexpected trend in S3—its reversion to shear failure despite higher capacity—raises questions about the balance between beam and joint strengthening. This could indicate a threshold where extended UHPSFRC length shifts critical stresses back to the joint, reducing ductility. Such behavior necessitates integrated beam-column design to avoid unintended stress concentrations, particularly in real structures with variable axial loads or reinforcement layouts. The increased peak loads in S2 and S3 (19% and 25% over S1, respectively) suggest potential for reducing transverse reinforcement, but S3's outcome cautions against over-reliance on length alone without considering joint confinement.

Environmental conditions during curing (23 ± 2°C, 95 ± 5% humidity) and testing (25 ± 3°C, 60 ± 10% humidity) were controlled to minimize their impact on material behavior and test outcomes. These stable conditions ensured consistent concrete hydration and UHPSFRC fiber performance during curing, while preventing moisture or thermal-induced variations in crack propagation and strain during testing. Analysis of strain and crack data showed no significant anomalies attributable to environmental fluctuations, as confirmed by comparing results with preliminary ABAQUS simulations conducted under assumed constant conditions (25°C, 60% humidity). This control supports the reliability of the observed differences between S1, S2, and S3, attributing them primarily to UHPSFRC strengthening rather than external variables.

These results advocate for UHPSFRC as a viable seismic retrofitting strategy, with S2's balanced performance meeting FEMA 273 criteria for enhanced seismic resilience [33]. Future parametric studies and numerical modeling could refine optimal strengthening lengths, exploring variables like fiber volume, joint aspect ratio, and axial load effects to ensure consistent ductility across diverse applications.

5. Conclusion

This study underscores the transformative role of ultra-high performance steel fiber reinforced concrete (UHPSFRC) in bolstering the seismic resilience of reinforced concrete (RC) exterior joints, offering a leap forward from conventional designs prone to brittle shear failure. The experimental results reveal a clear hierarchy of performance: the control specimen (S1) succumbed to shear collapse at 185.8 kN, while UHPSFRC-strengthened specimens achieved higher capacities—S2 at 220.8 kN with a ductile beam failure, and S3 at 231.4 kN, though reverting to shear failure. These outcomes highlight UHPSFRC's ability to enhance load-bearing capacity and control crack development, with S2's 800 mm strengthening length emerging as an optimal configuration that balances strength and ductility. By shifting damage to the beam and eliminating the need for joint stirrups, UHPSFRC addresses longstanding construction challenges, such

as reinforcement congestion, while improving seismic energy dissipation—a critical advantage for retrofitting aging infrastructure in earthquake-prone regions. The optimality of 800 mm stems from its alignment with the beam's plastic hinge zone, enabling controlled flexural yielding while preserving joint stability, whereas the 1025 mm length in S3 over-stiffened the beam, redirecting failure to the joint despite a higher ultimate capacity. Conversely, S3's performance suggests that extending the strengthening length beyond a certain threshold (1025 mm here) may over-stiffen structural elements, compromising the intended ductility benefits. This research advances the field by pinpointing a practical design parameter—strengthening length—that can guide engineers in optimizing UHPSFRC applications for robust RC frames. The findings position UHPSFRC as a promising alternative to traditional retrofitting techniques, aligning with global efforts to enhance structural safety against seismic threats.

Looking ahead, this study lays a robust foundation for integrating UHPSFRC into mainstream seismic design practices, building on its demonstrated benefits in capacity enhancement and construction simplification. While the superior performance of S2 suggests immediate applicability, the nuanced behavior of S3 calls for further exploration to refine UHPSFRC's limits and ensure consistent ductility across diverse conditions. Future research should prioritize parametric studies—examining variables like fiber volume, joint aspect ratios, and axial load variations—to establish comprehensive design guidelines. Numerical modeling could complement these efforts, offering predictive insights into UHPSFRC's behavior under a wider range of scenarios, while long-term durability tests under cyclic loading would validate its viability in real-world settings. Cost-benefit analyses and field trials are also essential to accelerate UHPSFRC's adoption, particularly for pre-modern structures lacking seismic detailing. By synthesizing experimental evidence with practical implications, this work bridges material innovation and structural engineering, advocating for strategic UHPSFRC deployment to meet the evolving demands of seismic resilience. These advancements pave the way for standardized approaches that could redefine how RC frames are designed and retrofitted, ensuring safer, more sustainable infrastructure in an increasingly seismic world.

6. Declarations

6.1. Data Availability Statement

Data sharing is not applicable to this article.

6.2. Funding

The author received no financial support for the research, authorship, and/or publication of this article.

6.3. Conflicts of Interest

The author declares no conflict of interest.

7. References

[1] Tuken, A., Abbas, Y. M., & Siddiqui, N. A. (2023, October). Efficient prediction of the load-carrying capacity of ECC-strengthened RC beams–an extra-gradient boosting machine learning method. Structures, 56, 105053. doi:10.1016/j.istruc.2023.105053

[2] Sun, B., Li, P., Wang, D., Ye, J., Liu, G., & Zhao, W. (2023). Evaluation of mechanical properties and anisotropy of 3D printed concrete at different temperatures. Structures 51, 391-401. doi:10.1016/j.istruc.2023.03.045.

[3] Huang, Y., Wu, J. H., Yang, S. K., Wang, L. B., & Ma, F. (2024). Multiple blast resistance enhancement through negative-mass meta-honeycombs with multi-resonator. Composite Structures, 330, 117845. doi:10.1016/j.compstruct.2023.117845.

[4] Feng, J., Rohaizat, R. E. B., & Qian, S. (2022). Polydopamine@ carbon nanotube reinforced and calcium sulphoaluminate coated hydrogels encapsulating bacterial spores for self-healing cementitious composites. Cement and Concrete Composites, 133, 104712. doi:10.1016/j.cemconcomp.2022.104712.

[5] Zheng, W., You, S., Yao, Y., Ren, N., Ding, B., Li, F., & Liu, Y. (2023). Sustainable Generation of Sulfate Radicals and Decontamination of Micropollutants via Sequential Electrochemistry. Engineering, 30, 144–152. doi:10.1016/j.eng.2022.12.005.

[6] Qin, D., You, X., Wang, H., Liu, Y., Shi, Y., Wang, N., Zhang, X., Feng, C., Liu, Y., Kong, M., Cheng, X., Bi, S., & Chen, X. (2023). Natural micropatterned fish scales combing direct osteogenesis and osteoimmunomodulatory functions for enhancing bone regeneration. Composites Part B: Engineering, 255, 110620. doi:10.1016/j.compositesb.2023.110620.

[7] Yoo, D.-Y., Oh, T., & Banthia, N. (2022). Nanomaterials in ultra-high-performance concrete (UHPC) – A review. Cement and Concrete Composites, 134, 104730. doi:10.1016/j.cemconcomp.2022.104730.

[8] Zainal, S. I. S., Hejazi, F., & Rashid, R. S. (2021). Enhancing the performance of knee beam–column joint using hybrid fibers reinforced concrete. International Journal of Concrete Structures and Materials, 15, 1-28. doi:10.1186/s40069-021-00457-w.

[9] Sai Kubair, K., & Kalyana Rama, J. S. (2021). Seismic Performance of UHPFRC-Strengthened RC Beam–Column Joints Using Damage Plasticity Model—A Numerical Study. Recent Advances in Earthquake Engineering: Select Proceedings of VCDRR, 371-383. doi:10.1007/978-981-16-4617-1_30.

[10] Zhou, G., Tang, F., Li, G., & Li, H. N. (2024). Gold-sputtered LPG fiber sensor pulse electroplated with iron-carbon for monitoring passivation and depassivation of carbon steel in concrete pore solutions. Cement and Concrete Composites, 147, 105432. doi:10.1016/j.cemconcomp.2024.105432.

[11] Shoukry, M. E., Tarabia, A. M., & Abdelrahman, M. Z. (2022). Seismic retrofit of deficient exterior RC beam-column joints using steel plates and angles. Alexandria Engineering Journal, 61(4), 3147–3164. doi:10.1016/j.aej.2021.08.048.

[12] Khodaei, M., Saghafi, M. H., & Golafshar, A. (2021). Seismic retrofit of exterior beam-column joints using steel angles connected by PT bars. Engineering Structures, 236, 112111. doi:10.1016/j.engstruct.2021.112111.

[13] Bezerra, A. K. L., Melo, A. R. S., Freitas, I. L. B., Babadopulos, L. F. A. L., Carret, J. C., & Soares, J. B. (2023). Determination of modulus of elasticity and Poisson's ratio of cementitious materials using S-wave measurements to get consistent results between static, ultrasonic and resonant testing. Construction and Building Materials, 398, 132456. doi:10.1016/j.conbuildmat.2023.132456.

[14] de Souza, T. B., Medeiros, M. H. F., Araújo, F. W. C., & de Melo Neto, A. A. (2023). The influence of expanded polystyrene granules on the properties of foam concrete. Materials and Structures/Materiaux et Constructions, 56(1), 45. doi:10.1617/s11527-023-02109-9.

[15] Huang, Y., Grünewald, S., Schlangen, E., & Luković, M. (2022). Strengthening of concrete structures with ultra-high performance fiber reinforced concrete (UHPFRC): A critical review. Construction and Building Materials, 336, 127398. doi:10.1016/j.conbuildmat.2022.127398.

[16] Xu, D., Tang, J., Hu, X., Yu, C., Han, F., Sun, S., ... & Liu, J. (2023). The influence of curing regimes on hydration, microstructure and compressive strength of ultra-high performance concrete: A review. Journal of Building Engineering, 76, 107401. doi:10.1016/j.jobe.2023.107401.

[17] Lei, D. Y., Guo, L. P., Chen, B., Curosu, I., & Mechtcherine, V. (2019). The connection between microscopic and macroscopic properties of ultra-high strength and ultra-high ductility cementitious composites (UHS-UHDCC). Composites Part B: Engineering, 164, 144-157. doi:10.1016/j.compositesb.2018.11.062.

[18] Amran, M., Murali, G., Makul, N., Tang, W. C., & Alluqmani, A. E. (2023). Sustainable development of eco-friendly ultra-high performance concrete (UHPC): Cost, carbon emission, and structural ductility. Construction and Building Materials, 398, 132477. doi:10.1007/s40069-016-0157-4.

[19] Li, W., Lu, Y., Wang, P., Jiang, Y., Wang, L., Shi, T., & Zheng, K. (2023). Comparative study of compressive behavior of confined NSC and UHPC/UHPFRC cylinders externally wrapped with CFRP jacket. Engineering Structures, 292, 116513. doi:10.1016/j.engstruct.2023.116513.

[20] Chen, S. Z., Feng, D. C., Wang, W. J., & Taciroglu, E. (2022). Probabilistic machine-learning methods for performance prediction of structure and infrastructures through natural gradient boosting. Journal of Structural Engineering, 148(8), 04022096. doi:10.1061/(asce)st.1943-541x.0003401.

[21] Diab, Z., Do, D. P., Rémond, S., & Hoxha, D. (2023). Probabilistic prediction of structural failure during 3D concrete printing processes. Materials and Structures, 56(4), 73.. doi:10.1617/s11527-023-02167-z.

[22] Sarraz, A., Nakamura, H., Kanakubo, T., Miura, T., & Kobayashi, H. (2022). Bond behavior simulation of deformed rebar in fiber-reinforced cementitious composites using three-dimensional meso-scale model. Cement and Concrete Composites, 131, 104589. doi:10.1016/j.cemconcomp.2022.104589.

[23] Wille, K., Naaman, A. E., El-Tawil, S., & Parra-Montesinos, G. J. (2012). Ultra-high performance concrete and fiber reinforced concrete: achieving strength and ductility without heat curing. Materials and structures, 45, 309-324. doi:10.1617/s11527-011-9767-0.

[24] Fehling, E., Schmidt, M., Walraven, J., Leutbecher, T., & Fröhlich, S. (2014). Ultra-high performance concrete UHPC. Ernst & Sohn: Berlin, Germany, 25-32. doi:10.1002/9783433604076.

[25] Chen, Z., Zhang, H., Yang, X., Leng, Z., & Tang, Y. (2024). Cooling efficiency of thermochromic asphalt pavement material and its contribution to field performance enhancement of asphalt mixture. Construction and Building Materials, 411, 134562. doi:10.1016/j.conbuildmat.2023.134562.

[26] Sitong, W., Jinghua, Z., Chao, Z., Guanghui, T., Quangeng, L., & Qing, S. (2022). Ultimate strengths of triple-ring-stiffened tube-gusset X-joints considering the effect of chord load. Structures, 46, 233–245. doi:10.1016/j.istruc.2022.10.067.

[27] Valcuende, M., Lliso-Ferrando, J. R., Ramón-Zamora, J. E., & Soto, J. (2021). Corrosion resistance of ultra-high performance fibre-reinforced concrete. Construction and Building Materials, 306, 124914. doi:10.1016/j.conbuildmat.2021.124914.

[28] Shao, Y., Tich, K. L., Boaro, S. B., & Billington, S. L. (2022). Impact of fiber distribution and cyclic loading on the bond behavior of steel-reinforced UHPC. Cement and Concrete Composites, 126, 104338. doi:10.1016/j.cemconcomp.2021.104338

[29] TCVN 197-1:2014. (2014). Metallic materials – Tensile testing – Part 1: Method of test at room temperature. Ministry of Science and Technology, Vietnam. (In Vietnamese).

[30] TCVN 1651-2:2008. (2008). Steel for reinforcement of concrete – Part 2: Ribbed bars. Construction Publishing House, Hanoi, Vietnam. (In Vietnamese).

[31] Ghasemi, M., Khorshidi, H., & Fanaie, N. (2021). Performance evaluation of RC-MRFs with UHPSFRC and SMA rebars subjected to mainshock-aftershock sequences. Structures, 32, 1871-1887. doi:10.1016/j.istruc.2021.02.058.

[32] Xiong, X., Wei, Z., Zhang, D., Liu, J., Xie, Y., & He, L. (2025). An Experimental Study on the Seismic Performance of New Precast Prestressed Concrete Exterior Joints Based on UHPC Connection. Buildings, 15(5), 729. doi:10.3390/buildings15050729.

[33] CSA S806:12. (2022). Canadian Standards Association (CSA). (2012). Design and Construction of Building structures with Fibre-Reinforced Polymer, CAN/CSA S806-12. Canadian Standards Association, Toronto, Canada.